Probing the mechanical properties of seismically active crust with space geodesy: Study of the co-seismic deformation due to the 1992 M_w7.3 Landers (southern California) earthquake

Yuri Fialko

Institute of Geophysics and Planetary Physics, Scripps Institution of Oceanography, University of California San Diego, La Jolla, California

Abstract. The co-seismic deformation due to the 1992 M_w7.3 Landers earthquake, Southern California, is investigated using Synthetic Aperture Radar (SAR) and Global Positioning System (GPS) measurements. The ERS-1 satellite data from the ascending and descending orbits are used to generate contiguous maps of three orthogonal components (East, North, Up) of the co-seismic surface displacement field. The co-seismic displacement field exhibits symmetries with respect to the rupture plane that are suggestive of a linear relationship between stress and strain in the crust. Interferometric SAR data show small-scale deformation on nearby faults of the Eastern California Shear Zone. Some of these faults (in particular, the Calico, Rodman, and Pinto Mountain faults) were also subsequently strained by the 1999 M_w7.1 Hector Mine earthquake. I test the hypothesis that the anomalous fault strain represents essentially an elastic response of kilometer-scale compliant fault zones to stressing by nearby earthquakes [*Fialko et al.*, 2002]. The co-seismic stress perturbations due to the Landers earthquake are computed using a slip model derived from inversions of the InSAR and GPS data. Calculations are performed for both homogeneous and transversely isotropic half-space models. The compliant zone model that best explains the deformation on the Calico and Pinto Mountain faults due to the Hector Mine earthquake successfully predicts the co-seismic displacements on these faults induced by the Landers earthquake. Deformation on the Calico and Pinto Mountain faults implies about a factor of two reduction in the effective shear modulus within the ~ 2 km wide fault zones. The depth extent of the low rigidity zones is poorly constrained, but is likely in excess of a few kilometers. The same type of structure is able to explain high gradients in the radar line of sight displacements observed on other faults adjacent to the Landers rupture. In particular, the Lenwood fault north of the Soggy Lake has likely experienced a few centimeters of left-lateral motion across < 1 km wide compliant fault zone having the rigidity reduction of more than a factor of two. The inferred compliant fault zones are interpreted to be a result of extensive damage due to past earthquakes.

1. Introduction

Since the introduction of the elastic rebound theory almost a century ago [*Reid*, 1910], the idealization of the

Earth crust as an elastic-brittle solid has been widely used to describe the static and dynamic deformation fields due to earthquakes [e.g., *Vvedenskaya*, 1959; *Aki and Richards*, 1980; *Okada*, 1985; *Kostrov and Das*, 1988; *Dahlen and Tromp*, 1998]. Yet, direct observational constraints on the in situ constitutive behavior of crustal rocks (especially in the near field of seismic sources) are scarce. Over the last decade, advances in space geodetic techniques, in particular, the use of the Interferometric Synthetic Aperture Radar (InSAR) and development of dense Global Positioning System (GPS) in seismically active areas have allowed a detailed description of surface deformation due to shallow crustal earthquakes [e.g., *Massonnet et al.*, 1993; *Hudnut et al.*, 1994; *Freymueller et al.*, 1994; *Peltzer et al.*, 1998a; *Fialko et al.*, 2001b; *Simons et al.*, 2002; *Jonsson et al.*, 2002]. The spatially dense measurements of the co-seismic deformation may be used to refine our knowledge of the bulk mechanical properties of the Earth crust. For example, the InSAR observations of the 1997 M_w7.6 Manyi (Tibet) earthquake were interpreted as indicating the stress dependence of the elastic moduli of the host rocks [*Peltzer et al.*, 1998a], while a more complete data set from the 1999 M_w7.1 Hector Mine earthquake was found to be more consistent with the assumption of linear elasticity [*Fialko et al.*, 2001b]. InSAR observations also revealed wide-spread aseismic deformation on faults adjacent to the mainshock rupture, with some faults experiencing apparently "backward" motion due to nearby earthquakes [*Price and Sandwell*, 1998; *Sandwell et al.*, 2000; *Wright et al.*, 2001; *Fialko et al.*, 2001b, 2002]. The proposed explanations for strain localization on neighboring faults include shallow sub-surface slip induced by either the dynamic or static co-seismic stress changes [e.g., *Sandwell et al.*, 2000; *Wright et al.*, 2001], and a predominantly elastic response of the macroscopic compliant fault zones with significant (a factor of two) reductions in the effective shear modulus [*Fialko et al.*, 2002]. An ultimate test of these hypotheses requires detailed seismic and geodetic studies of the fault zone properties. In this paper I investigate the co-seismic deformation due to the 1992 M_w 7.3 Landers earthquake in southern California. In a companion paper [*Fialko*, 2004] the inferred slip model and co-seismic stress perturbations are used to investigate the mechanics of post-seismic deformation.

2. Data overview

The Landers event was the first large earthquake captured by the space-borne interferometric SAR (synthetic aperture radar). Some aspects of surface deformation due to the Landers earthquake have been previously discussed [e.g., *Massonnet et al.*, 1993; *Zebker et al.*, 1994; *Price and Sandwell*, 1998; *Hernandez et al.*, 1999], but a comprehensive analysis including all the available geodetic data has not yet been attempted. The Landers earthquake occurred shortly after the European Space Agency satellite ERS-1 has begun its mission, and only few pre-earthquake acquisitions are available. Location of the earthquake rupture, and radar scenes used in this study are shown in Figure 1. Most previous studies have used the co-seismic interferograms from the descending orbit (track 399). The InSAR data from only one look direction do not uniquely describe the surface displacement field, especially in the presence of both horizontal and vertical components of deformation [e.g., *Burgmann et al.*,

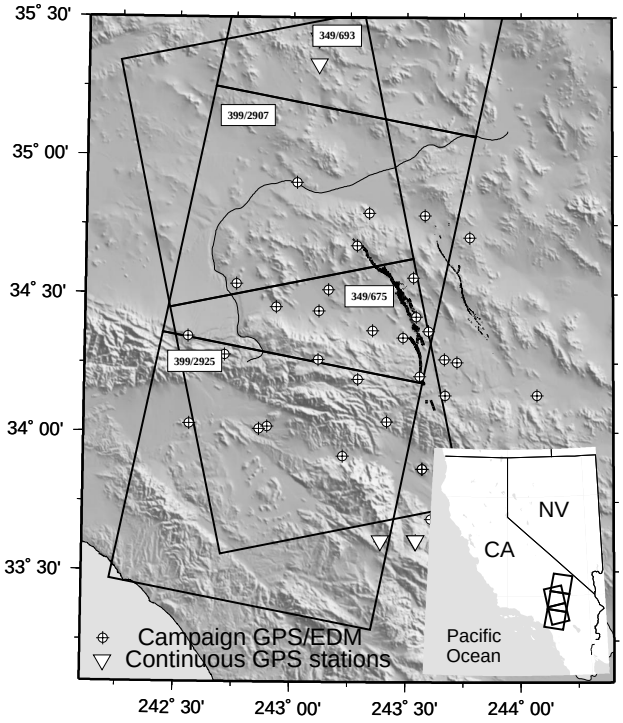

Figure 1. Shaded relief map of the area of study. Surface rupture of the Landers earthquake is shown by a thick black wavy line. Thin wavy line shows surface rupture of 1999 Hector Mine earthquake. Solid squares denote ERS radar scenes for the ascending (track 349, frames 675 and 693), and descending (track 399, frames 2889, 2907, and 2925) orbits. White arrows indicate the satellite look direction. Inverted triangles and crossed circles show positions of continuous and campaign-style GPS stations, respectively.

2000; *Fialko et al.*, 2001b]. To resolve the ambiguity between the horizontal and vertical displacements, I complement the InSAR data from the descending orbit with a co-seismic interferogram from the ascending orbit (track 349, see Figure 1). In addition to the interferometric line of sight measurements, I use the amplitude of the radar backscatter to derive the azimuthal offset (AZO) maps from both the ascending and descending orbits. The AZO data are obtained by cross-correlating the backscatter images obtained before and after the earthquake. The cross-correlation allows one to estimate the horizontal motion of individual pixels along the satellite track. Stability of the reflective properties of the ground in the Mojave desert gives rise to a deeply sub-pixel accuracy of the azimuthal offsets [e.g., *Fialko et al.*, 2001b; *Simons et al.*, 2002]. The InSAR data that most tightly bracket the earthquake date consist of radar acquisitions made on April 24 - August 7 (descending orbit), and May 26 - June 30, 1992 (ascending orbit). Note that the descending interferogram contains about 1.5 months of the post-seismic transient deformation; however, the latter is quite small (likely less than 10%) compared to the co-seismic signal [e.g., *Shen et al.*, 1994; *Savage and Svarc*, 1997; *Peltzer et al.*, 1998b]. In addition to the ERS SAR data, I use all available GPS and Electronic Distance Measurements (EDM) data of the co-seismic displacements. The point measurements of the displacement vectors used in this study include data from 8 continuous sites of the Southern California Permanent GPS Geodetic Array located within 150 km from the epicenter (white triangles in Figure 1) [*Bock et al.*, 1993], and 38 GPS and EDM sites surveyed in the campaign mode (crossed circles in Figure 1) [*Hudnut et al.*, 1994; *Freymueller et al.*, 1994].

The ERS SAR data were processed using a modified version 2.2 of the Jet Propulsion Laboratory (JPL)/Caltech software package ROI_PAC. The topographic contribution to the interferometric phase was removed using the digital elevation data provided by the Space Shuttle Topography Mission (SRTM) [*Farr and Kobrick*, 2000]. Accurate topography data are essential for isolating the deformation signal, as the perpendicular baselines of the co-seismic interferometric pairs are not small (97 m for the descending pair, and 367 m for the ascending pair) [for details, see e.g. *Gabriel et al.*, 1989; *Goldstein et al.*, 1993; *Massonnet and Feigl*, 1998]. The nominal SRTM accuracy of the order of several meters [*Farr and Kobrick*, 2000; *Smith and Sandwell*, 2003] implies potential topographic errors in the LOS displacements of the order of millimeters for both the descending and ascending interferograms. After corrections for topography, the interferograms were filtered, unwrapped, mapped from the satellite Doppler coordinate system onto a geographic grid, and averaged over 8-by-8 pixel bins.

Figures 2a-d show the co-seismic line of sight displacements and azimuthal offsets from the ascending and descending orbits. White areas in the displacement maps in Figures 2a-d denote regions of decorrelation in the LOS displacement maps, and low signal-to-noise ratio in the AZO maps. Black wavy lines in Figure 2 show the geologically mapped fault trace. The decorrelated regions extend about 1-2 km off the surface rupture, presumably indicating a zone of high damage and ground disruption around the fault. The AZO data are less affected by severe changes in the reflective properties of the ground around the earthquake rupture, and provide useful information about the near-fault displacements. The accuracy of the AZO data estimated in the process of cross-correlation of the radar amplitude images is of the order of a few tens of centimeters, substantially less than the meter-scale co-seismic offsets along the fault [*Sieh et al.*, 1993].

2.1. 3-D co-seismic surface displacement field

The SAR data shown in Figures 2a-d provide continuous maps of ground motion from four different viewing geometries, and may be used to retrieve all three orthogonal components of the displacement field, $U_i(e, n)$, where $i = e, n, v$, correspond to the East, North, and vertical coordinates [*Fialko et al.*, 2001b]. The scalar LOS and AZO measurements d at each pixel of the geo-referenced radar image represent a projection of the total displacement vector $\mathbf{U}$ (averaged over that pixel) onto some direction characterized by a unit view vector $\mathbf{v}$ [e.g., *Massonnet and Feigl*, 1998; *Burgmann et al.*, 2000; *Rosen et al.*, 2000], $d = \mathbf{U} \cdot \mathbf{v} + \delta$, where δ is the associated measurement error. The unit vector $\mathbf{v}$ corresponds to the direction from the back-scattering pixel on the ground toward the satellite for the LOS (interferometric phase) measurements, and the satellite heading for the AZO (cross-correlated amplitude) measurements. The explicit expressions for the components of $\mathbf{v}$ in terms of the satellite heading and radar incidence angles for the right-looking ERS satellites may be found, e.g., in *Fialko et al.* [2001b]. The measurement error δ consists of contributions from an imprecise knowledge of satellite orbits, path effects (e.g., variability in atmospheric conditions, most notably the water content), incorrect DEM, spurious phase unwrapping, satellite clock drift, etc. Except for the orbital errors, all of the above contributions are assumed to be small compared to the co-seismic signal, and con-

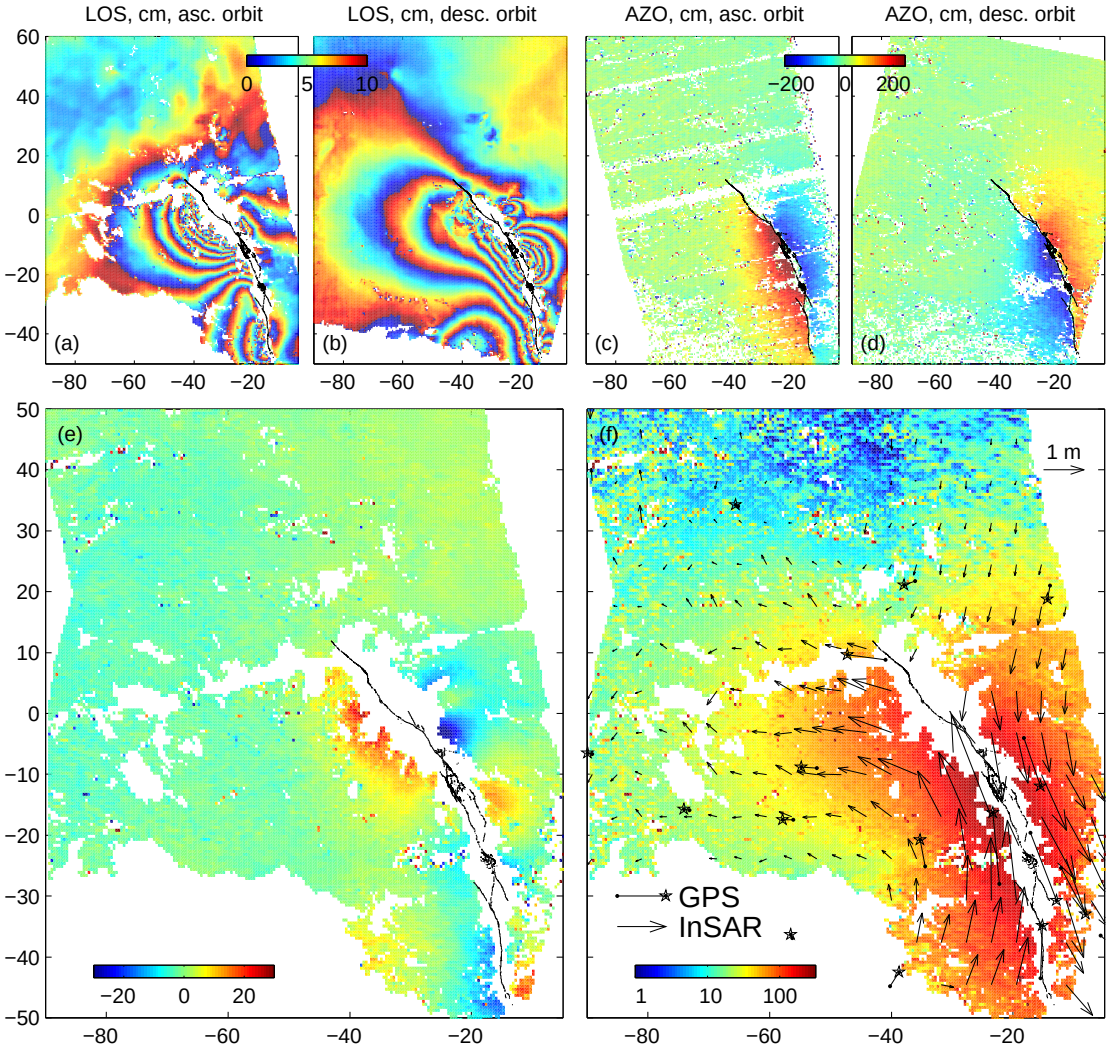

Figure 2. InSAR data used in this study. In all figures origin corresponds to the epicenter of the Hector Mine earthquake (116.27°W, 34.595°N). (a) Interferogram for the time period May 26-June 30, 1992, ascending orbit. (b) Interferogram for the time period April 24-August 7, 1992, descending orbit. The LOS displacements have been re-wrapped with the fringe cycle of 10 cm. Arrows show the satellite look direction. Azimuthal offsets, in cm, from the (c) ascending, and (d) the descending orbits. (e) Vertical and (f) horizontal components of the surface displacement field derived from the InSAR data. Arrows show the sub-sampled horizontal displacements, and starred arrows denote the GPS/EDM measurements.

sequently neglected. The orbital errors may give rise to long-wavelength "ramps" superimposed on the co-seismic displacement maps (for both the LOS and AZO data). In principle, it is possible to estimate the orbital errors from the InSAR data alone, given data from more than three different viewing geometries. Because of the relatively low accuracy of the AZO data, here the orbital errors are estimated from a joint inversion of the available SAR and GPS data for a low-resolution earthquake slip model, and best-fitting planar ramps [e.g., *Fialko et al.*, 2001b; *Simons et al.*, 2002, also, see Section 3 and Appendix A].

After subtracting the deduced orbital corrections the data shown in Figures 2a-d are inverted for a three-component co-seismic vector displacement field $\mathbf{U}$. For each ground pixel that has the LOS data from both orbits, and AZO datum from at least one orbit, I solve a linear system of equations $\mathbf{U} \cdot \mathbf{v} = d$ with the corresponding coefficients of the view vector $\mathbf{v}$. If data from all four projections are available, the components of $\mathbf{U}$ are found by solving an overdetermined system of equations using a method of least squares. Prior to solving an overdetermined system, both the left and right sides of each equation are normalized by an estimated measurement error (an a-priori error of 1 cm is assumed for the LOS data). Vertical and horizontal components of the co-seismic displacement field yielded by the inversion are shown in Figures 2e-f. The imaging geometry of the ERS satellites, and the orientation of the Landers rupture are such that the azimuthal offsets are mostly sensitive to the North-South component of deformation, while the line of sight measurements for both orbits are strongly sensitive to the vertical, modestly sensitive to the East-West, and weakly sensitive to the North-South component of deformation. Figure 2f shows the magnitude (color) and direction (arrows) of a horizontal component of the displacement field. Also shown in Figure 2f are the co-seismic GPS and EDM observations of horizontal displacements [*Freymueller et al.*, 1994]. Although the GPS data were used to calculate the orbital correction δ, a comparison between the displacement field inferred from the SAR data, and GPS observations is non-trivial, as our decomposition of the SAR measurements into orthogonal displacement components is not constrained by the GPS data. Also, the inferred magnitude of δ is small compared to the observed displacements within a few tens of kilometers from the surface rupture. Figure 3 compares components of the displacement vector U_i deduced from the SAR and GPS data, along with the corresponding measurement errors. Because the formal measurement errors for the SAR-derived displacement field are not available, I use the estimated errors of the AZO data, which likely dominate the quality of the solution. As one can see from Figures 2f and 3, the SAR and GPS measurements of co-seismic displacements are in overall agreement. This lends support to the assumption that the LOS and AZO data from both the ascending and descending orbits are sufficient to describe the co-seismic displacement field due to the Landers earthquake. A further analysis of surface deformation seen in Figures 2e-f is presented in Section 4.

3. Inversion of SAR and GPS data for slip distribution

As shown in the previous section, the SAR data from the Landers earthquake provide a nearly complete resolution of the surface deformation field. These data provide most useful constraints on the distribution of slip on faults ruptured during the earthquake. I invert all available SAR and GPS data for the slip model of the Landers earthquake using a constrained least squares minimization that includes iterations for the fault geometry. The initial guess of the fault geometry is made based on SAR observations (in particular, AZO data, see Figure 2c-d), field mapping of surface rupture [*Sieh et al.*, 1993], and the aftershock locations [*Hauksson et al.*, 1993]. The surface trace of the fault model is shown in Figure 4 along with the observed rupture trace and aftershocks. To account for the spatial complexity of the Landers rupture (Figure 4), the latter is approximated by six vertical rectangular fault segments. The width (down-dip dimension) of the fault segments is taken to be 15 km. In addition to the main Landers rupture, the model includes 3 additional segments representing a slip plane of the Big Bear aftershock, and antithetic faults adjacent to the Landers rupture north and south of the Iron Ridge (segments 7, 8 and 9 in Figure 4, respectively). Addition of these three segments is warranted by the initial inversions that showed systematic residuals due to the left-lateral motion on these auxiliary faults. To allow for a spatially heterogeneous slip on the fault segments, I subdivide each segment into smaller slip patches such that the patch size increases from about 1 km (both along-strike and down-dip) at the top of the fault to ~ 5 km at the bottom of the fault approximately in a geometric progression such that the model resolution is essentially independent of depth [Appendix A; also, see *Simons et al.*, 2002; *Jacobs et al.*, 2002]. Besides naturally addressing a trade-off between the source size and the source strength intrin-

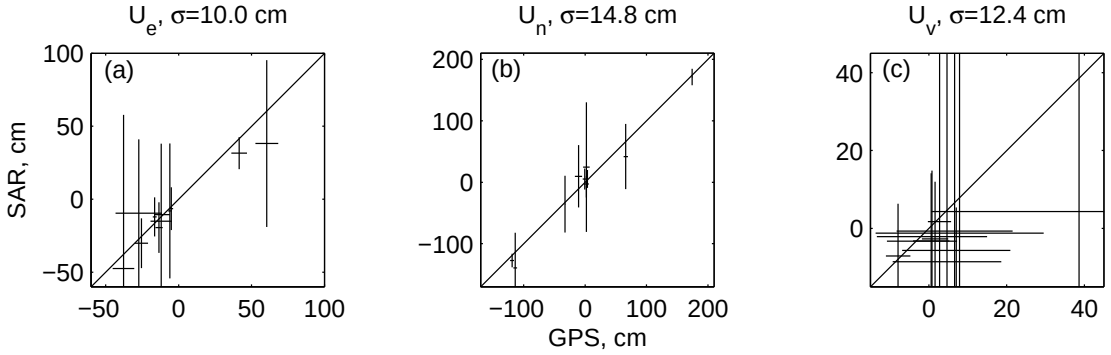

Figure 3. A comparison between the SAR-derived co-seismic displacement field and GPS observations. SAR data represent average displacements over ~ 0.5 km $\times 0.5$ km areas that contain the GPS stations. Horizontal bars show errors in the GPS solutions, and vertical bars show errors in the AZO data. σ denotes the rms misfit for each component of the displacement vector U_i.

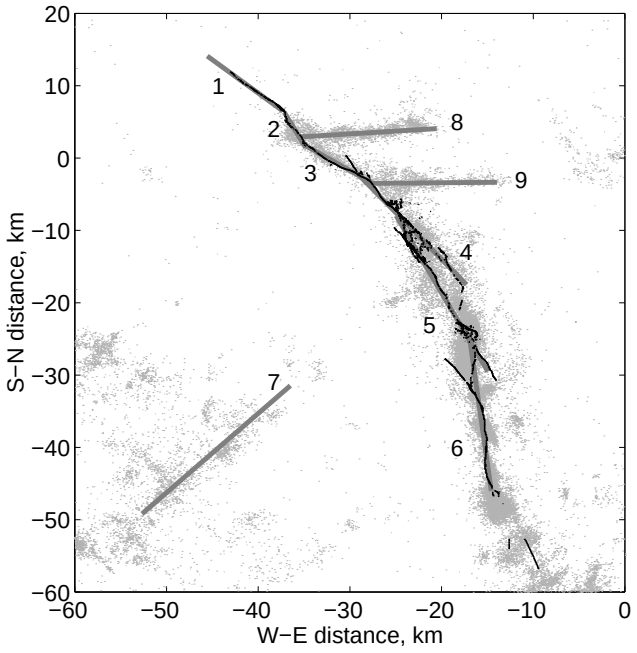

Figure 4. Fault model used to simulate the Landers rupture. Shown are the top edges of the model subfaults (dark grey lines) superimposed on the mapped fault rupture (black wavy line) and aftershocks (light grey dots).

sic for deformation sources that are small compared to their depth [e.g., *Fialko and Simons*, 2000], the variable patch parameterization reduces the problem size and the simulation time.

The computational task is further facilitated by subsampling of the SAR data using a recursive quad-tree algorithm [e.g., *Simons et al.*, 2002; *Jonsson et al.*, 2002]. Initially, the data are sampled on a relatively sparse regular grid with spacing of ~ 7 km. Closer than 50 km to the fault, the sampling algorithm selects additional data points that are necessary and sufficient to restore the original data set with prescribed accuracy by linear interpolation. The sub-sampled SAR data used in the inversion are shown in Figures 5a-d. Spacing between the selected data points is indicative of the degree of averaging for each selected datum; each datum represents a mean of all pixels within the corresponding quad. The details of modeling are described in Appendix A. Geometric parameters of sub-faults used in the inversion are given in Table 1.

Slip models are derived for the cases of homogeneous and horizontally-stratified elastic half-spaces. For the homogeneous half-space model the slip patches are approximated by finite rectangular dislocations [e.g., *Okada*, 1985]. For the layered half-space model the slip patches are approximated by arrays of point dislocations with a constant slip. The surface deformation of a layered half-space was simulated using numerical codes of *Zhu and Rivera* [2002] and *Wang et al.* [2003]. Both techniques gave rise to essentially identical results. The layered half-space solutions presented below are obtained using a numerical scheme of *Wang et al.* [2003]. The rigidity structure used in the layered

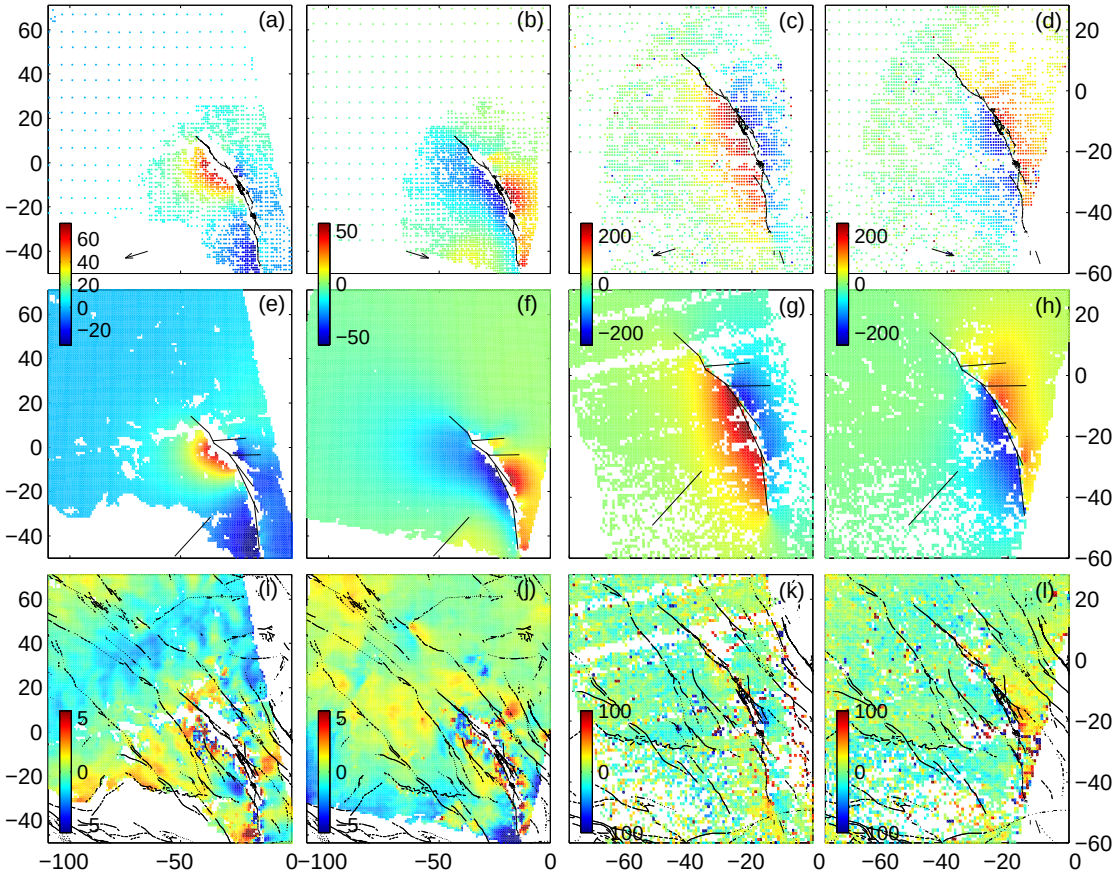

Figure 5. (a)-(d) Sub-sampled InSAR data used in the inversion (the LOS data include parts of interferograms not shown in the pictures, sampled at a base spacing of ∼7 km). (e)-(h) Best-fitting models. (i)-(l) Residuals after subtracting the best-fitting models from the data.

Table 1. Landers fault model used in the inversion

Parameters	Sub-faults								
	1	2	3	4	5	6	7	8	9
x_o, km	-41.44	-35.98	-31.18	-23.14	-19.95	-15.79	-44.57	-28.00	-20.75
y_o, km	10.32	-3.89	-0.88	-9.93	-18.74	-35.20	-40.32	3.5	-3.43
Length L, km	11.20	5.46	9.32	19.13	23.76	21.80	24.00	15.00	13.57
Strike, deg	133	155	125	142	155	174	42	86	89
Dip, deg	89	90	90	90	90	90	95	90	90

All faults have width (down-dip dimension) of 15 km, with top edges intersecting the surface. Coordinates x_o, y_o correspond to centers of the top edges of the faults. Origin is taken to be at the epicenter of the Hector Mine earthquake.

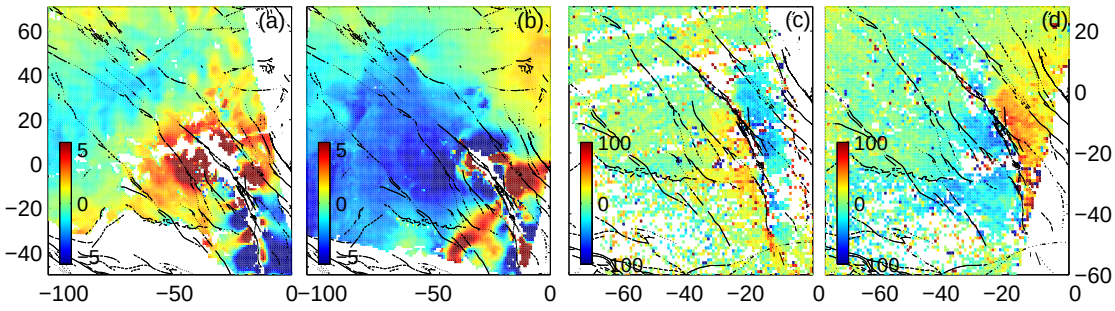

Figure 7. Residuals after subtracting the synthetic SAR data predicted by the *Wald and Heaton* [1994] model from the observed SAR data (Figures 2a-d). Notation is the same as in Figure 2.

half-space simulations is inferred from the seismic velocity model of the Mojave desert [*Jones and Helmberger*, 1998], and schematically shown in Figure 6. Inversions indicate that the data can be fit equally well assuming either the homogeneous or layered half-space elastic models, similar to the results of the Hector Mine study [*Simons et al.*, 2002]. The best-fitting SAR synthetics, and the difference between the observed data and our best-fitting model for the homogeneous half-space are shown in Figure 5. The derived slip models are a significant improvement over previous inversions that relied only on a fraction of the available geodetic data. For example, Figure 7 shows a misfit between the SAR observations and the predictions of the *Wald and Heaton* [1994] model derived from the joint inversion of the teleseismic, strong motion, and GPS data. To ensure consistency, the synthetic LOS and AZO displacement maps are calculated assuming the regional velocity model used in the inversions of *Wald and Heaton* [1994]. A comparison of Figures 5i-l and 7a-d indicate that inversions of high-quality seismic data (including teleseismic and strong-motion records) for the rupture history may substantially benefit from incorporating the spatially dense space geodetic data. Because of the intrinsic trade-offs between the timing and location of slip in the time-dependent simulations, a joint inversion of seismic and geodetic data may be less effective than a separate inversion of seismic data alone that uses the static slip model as a constraint [*Hernandez et al.*, 1999].

Figure 8 shows the slip distribution for the best-fitting homogeneous half-space model, and Figure 9 shows the corresponding solution for the layered half-space model. The main difference between the two models is that the layered model predicts a somewhat greater slip at depth compared to the homogeneous half-space model, as expected [e.g., *Savage*, 1998]. Inversions of synthetic data suggest that the main features

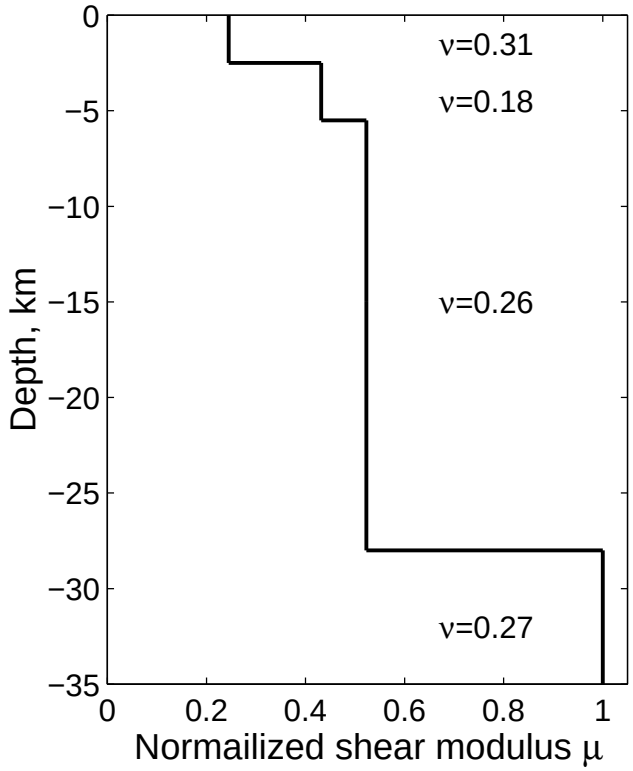

Figure 6. Variations in the elastic properties (shear modulus μ and Poisson ratio ν) as a function of depth as inferred from the seismic velocity model of *Jones and Helmberger* [1998]. The shear modulus is normalized by the modulus of the underlying half-space (mantle). Note that the surface displacements due to kinematic sources (e.g., dislocations) depend only on variations in the shear modulus with depth, and not on its absolute value.

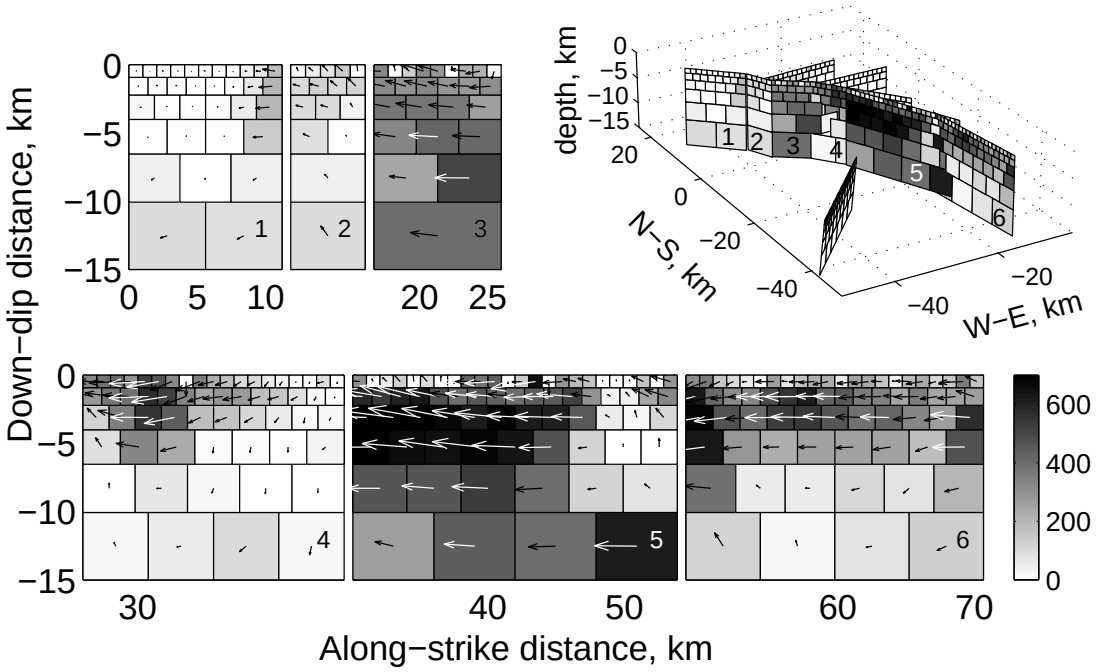

Figure 8. Slip distribution from the joint inversion of the SAR/GPS data for the homogeneous elastic half-space model. Shading intensity denotes the amplitude of the strike-slip displacements, and arrows show the direction of slip on the western side of the Landers rupture, viewing from the west to the east.

of the slip models shown in Figures 8 and 9 are reasonably well resolved (Appendix B).

An objective test of the robustness of an inverse model is the ability of the latter to predict independent data. Figure 10 shows a comparison between the model predictions of the GPS and EDM data that were used in the inversion (Figure 10a), and independent (and somewhat more extensive) GPS data recently provided as part of the new SCEC crustal velocity map (Figure 10b). It is interesting to note that the preferred model on average exhibits a better agreement with the independent GPS data than with the GPS data used (albeit heavily down-weighted, see Appendix A) in the inversion. Results shown in Figure 10 illustrate that models that fit the SAR data from different satellite viewing geometries are likely to adequately characterize the surface displacement field. As one can see from Figure 10, the difference between the model predictions and any particular GPS dataset is less than the difference between the two independent GPS solutions. The surface offsets predicted by the models shown in Figures 8 and 9 have a roughly triangular distribution and high variability along the fault trace with a peak amplitude of ∼6 m, in good agreement with the field mapping results [*Sieh et al.*, 1993]. A geodetic moment calculated by summing the potencies (area times slip) of the fault patches, and multiplying the sum by the typical shear modulus of the Earth crust (3.3×10^{10} Pa) is 1.17×10^{20} N·m for the layered half-space model, and 1.03×10^{20} N·m for the homogeneous half-space model. These values are in general agreement with the moment estimates based on the inversions of teleseismic data [1.1×10^{20} N·m; *Kanamori et al.*, 1992], and geologic observations [0.9×10^{20} N·m; *Sieh et al.*, 1993], but is somewhat larger than the seismic moment inferred from inversions of the broadband body wave and strong motion data [0.8×10^{20}N·m; *Kanamori et al.*, 1992; *Wald and Heaton*, 1994]. Some of the discrepancy may be due to variations in the value of the shear modulus used in the moment calculations. Also, the scalar sum of geodetic moments of individual slip patches is likely to overestimate the seismic moment if the fault is not planar. In the latter case, a tensorial sum may be more appropriate for comparisons with the point source representations. Finally, the inferred slip distribution on the Landers rupture (Figure 9) is in general agreement with the dynamic rupture simulations that fit the seismic data [e.g., *Peyrat et al.*, 2001].

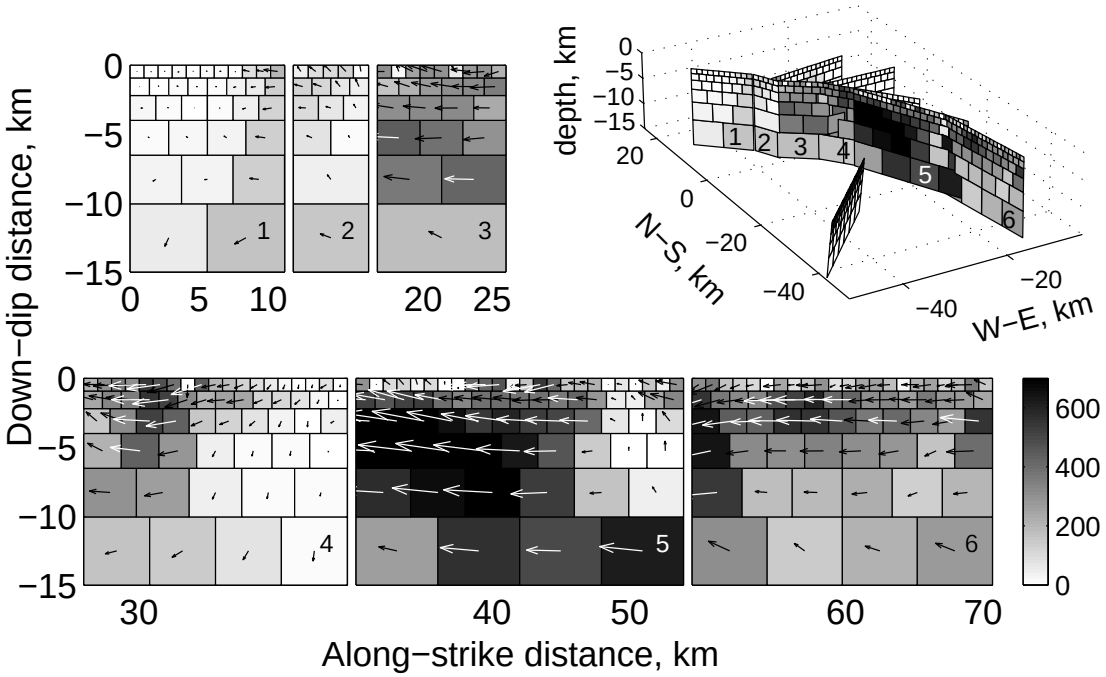

Figure 9. Slip distribution from the joint inversion of the SAR/GPS data for the layered elastic half-space model (Figure 6). Notation is the same as in Figure 8.

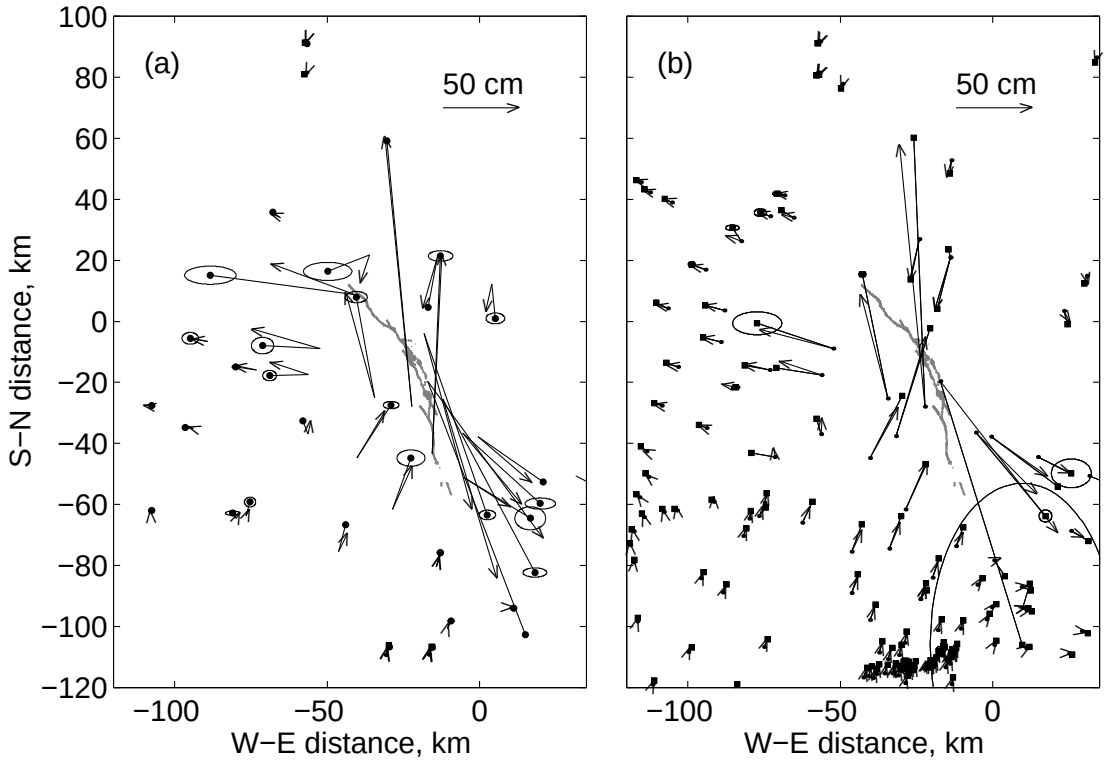

Figure 10. A comparison between the horizontal co-seismic displacements predicted by the best-fitting model (arrows), and observed with GPS (dotted lines). Ellipses denote the estimated errors in the GPS solutions. (a) GPS and EDM data (courtesy of Yehuda Bock and Jeff Freymueller) used in the inversion. (b) The Landers co-seismic GPS solutions from the SCEC crustal motion map CCM3 (`http://epicenter.usc.edu/cmm3/`).

Models shown in Figures 8 and 9 are based on a number of simplifications; in particular, they neglect possible lateral variations in the host rock rigidity. The fact that these models are able to satisfactory fit the data (Figures 5 and 10) suggests that the large-scale co-seismic deformation due to the Landers earthquake in general is consistent with the assumption of the transversely isotropic linearly elastic Earth's crust. At smaller scales, the systematic residuals having wavelength up to several km, and amplitude up to several centimeters (Figures 5i-j) imply that the assumption of either lateral homogeneity, or linear elasticity (or both) breaks down, provided that these residuals are due to surface deformation and not observation errors. In the next section I test the hypothesis that at least some residuals are correlated with the pre-existing faults and indicative of lateral variations in the elastic properties of the crust.

4. Co-seismic deformation induced by the Landers earthquake on nearby faults

The co-seismic strain concentration on faults adjacent to the Landers rupture has been documented by several studies [e.g., *Zebker et al.*, 1994; *Bodin et al.*, 1994; *Price and Sandwell*, 1998; *Rymer*, 2000], and generally explained in terms of shallow fault slip. However, the InSAR observations of co-seismic deformation due to the nearby 1999 Hector Mine earthquake have led *Fialko et al.* [2002] to conclude that at least in some cases the observed strain localization more likely results from the reduced elastic moduli within the fault zone, rather than induced slip. That is, the fault zones are compliant and therefore more strongly deformed by the co-seismic stress perturbations than the ambient crust. *Fialko et al.* [2002] inferred significant (about a factor of two) reductions in the shear modulus within kilometer-wide zones around several faults in the Eastern California Shear Zone, including the Calico, Rodman, and Pinto Mountain faults. The compliant fault zone hypothesis predicts that the sense of the along-strike displacements within the fault zone is controlled by the sense of the co-seismic shear stress changes. Similarly, the sign of vertical displacements is controlled by changes in the normal stress resolved on the fault plane (e.g., uplift in case of fault-normal compression, and subsidence in case of fault-normal extension). Patterns of the co-seismic surface deformation due to the Landers earthquake provide a good test for the compliant fault zone hypothesis because the fault zone model used to explain the anomalous fault strain due to the Hector Mine earthquake [*Fialko et al.*, 2002] should be able to predict the fault response to stressing by the Landers earthquake.

To isolate the small-scale signal that would be associated with the anticipated motion on the neighboring faults I high-pass filter the unwrapped co-seismic interferograms using a two-dimensional box-car filter with a cut-off wavelength of 7 km. Figure 11 shows the filtered interferograms from the descending and ascending orbits. The short-wavelength LOS displacements are quite noisy (presumably, due to atmospheric variability). Nonetheless, it is apparent from Figure 11 that several faults adjacent to the Landers rupture, including the Calico, Rodman, and Pinto Mountain faults, exhibit across-strike variations in the LOS displacements characteristic of the induced fault zone deformation. To verify whether the inferred anomalous fault strain is consistent with the compliant fault zone model, it is necessary to calculate the co-seismic stress perturbations on the target faults due to the Landers earthquake. I calculate the shear and normal stress changes due to the Landers earthquake using the slip models for the homogeneous and layered elastic half-space models shown in Figures 8 and 9. Figure 12 shows the stress changes in the layered half-space resolved on vertical faults striking 35°NW (i.e., the majority of faults in ECSZ, including the Calico and Rodman faults) at depth of 2 km. Additional calculations illustrating the co-seismic stress changes for various strikes and depths of the receiver faults are available on-line at `http://sioviz.ucsd.edu/~fialko/res_land.html`. The relative location of the target faults with respect to the nearby earthquake ruptures is favorable in that the co-seismic stress changes due to the Landers earthquakes in some cases are opposite in sign compared to the stress changes due the Hector Mine earthquake. For example, the Calico and Rodman faults experienced fault-normal extension due to the Landers earthquake (Figure 12b), and fault-normal compression due to the Hector Mine earthquake [*Fialko et al.*, 2002, see their figure 3b]. Similarly, the Pinto Mountain fault was extended by the Hector Mine earthquake, and compressed by the Landers earthquake. The response of the Pinto Mountain fault to the co-seismic stress perturbations is particularly instructive, as the normal stress changes dominate the shear stress changes for both earthquakes. In this case, the compliant fault zone model predicts that the satellite LOS displacements for both the ascending and descending orbits should be primarily sensitive to vertical deformation within the fault zone. A comparison of the high-pass filtered LOS displacements induced on the

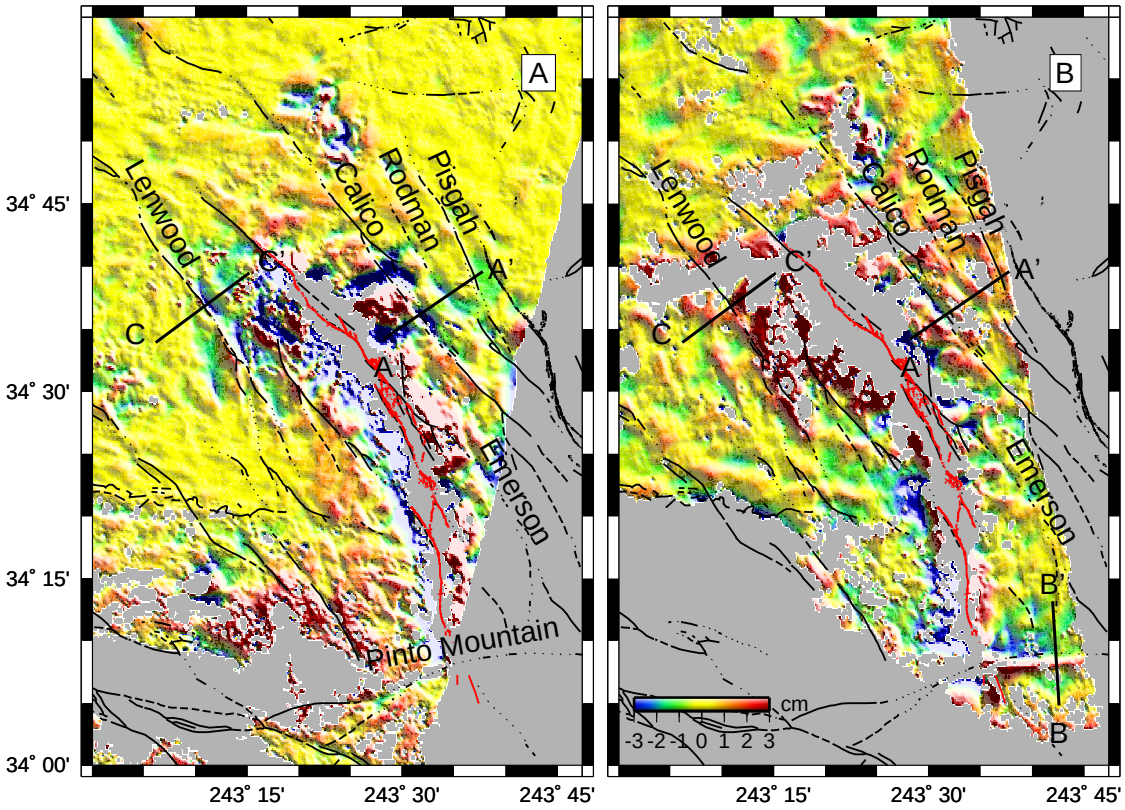

Figure 11. High-pass-filtered co-seismic interferograms from (a) the descending orbit, and (b) the ascending orbit. Colors and shading denote variations in the radar line of sight displacements. LOS displacements toward the satellite (decreases in the radar range) are taken to be positive.

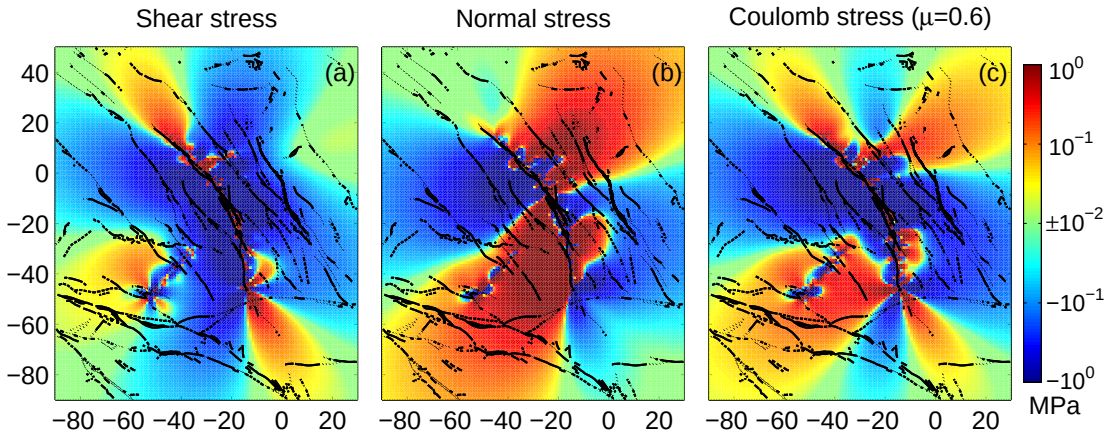

Figure 12. Static stress changes due to the Landers earthquake, in megapascals, on vertical faults striking 35°NW, at depth of 2 km. (a) Shear stress change. (b) Normal stress change. (c) Coulomb stress change. Extensional, and right-lateral shear and Coulomb stress changes are considered to be positive. Coulomb stress changes are computed assuming the coefficient of friction of 0.6. Horizontal coordinates are in km, with origin at the Hector Mine epicenter.

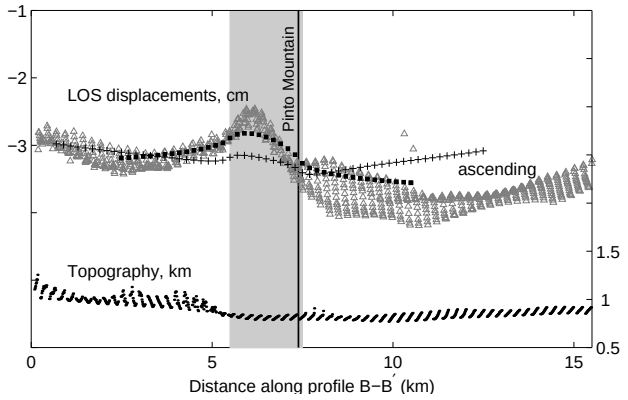

Figure 13. Results of finite element modeling of the compliant fault zone associated with the Pinto Mountain fault. The data (grey triangles) represent residual LOS displacements from the ascending interferogram (Figure 5i). Black symbols show the model predictions for a 2 km wide compliant fault zone that (i) extends to large depth (squares), and (ii) is restricted to the uppermost 2 km (pluses). The static fault-normal stress change due to the Landers earthquake is 0.6 MPa, and shear stress change is 0.4 MPa. The shaded interval denotes the extent of the fault zone, and black line denotes the position of the geologically mapped fault trace. The bottom curve shows the topography from the corresponding swath along BB′. The lack of correlation between the topography and anomalous LOS displacements suggests that the anomalies are not likely to be due to atmospheric errors.

Pinto Mountain fault by the Landers and Hector Mine earthquakes confirms these qualitative predictions: the segment of the Pinto Mountain fault that experienced subsidence during the Hector Mine earthquake [*Fialko et al.*, 2002, their figure 1b], has been uplifted during the Landers earthquake (Figure 11b).

To quantify the agreement between the observed LOS displacements and the model predictions, I compare the residual LOS displacements (Figures 5i-j) across the presumed compliant fault zones to the synthetic LOS displacements calculated using the fault zone properties inferred from the previous study of the Hector Mine earthquake [*Fialko et al.*, 2002]. The observed and modeled LOS displacements across the Pinto Mountain fault (see profile BB′ in Figure 11b) are shown in Figure 13. The data in Figure 13 represent the LOS displacements and topography within a 3-km wide swath centered on the profile BB′ (Figure 11b). The theoretical response of the compliant fault zone to the coseismic stressing is calculated using the 3-D finite element code ABAQUS. The computational domain consists of a low-rigidity parallelepiped welded to a stiffer block representing the ambient crust. All simulations assume a factor of two difference between the shear moduli of the fault zone and the ambient crust. The block representing the ambient crust is ten times wider than the low-rigidity zone. Because of the symmetry of the problem, the low-rigidity block corresponds to one half of the compliant fault zone. The left side of the low-rigidity block represents a symmetry plane, and is assumed to have zero horizontal displacements. A constant shear and normal stress that equal the inferred co-seismic stress perturbations on the fault zone are applied at the right side of the rigid block (i.e., parallel but opposite to the symmetry plane). To ensure no variations in stresses and displacements along the fault zone, periodic boundary conditions are applied at the front and back sides (i.e., vertical sides orthogonal to the interface between the soft and rigid blocks). Note that although the finite element model is fully three-dimensional, the solution is essentially a superposition of the plane strain deformation that depends only on the fault-normal stress, and the anti-plane strain deformation that depends only on the shear stress. The computational domain is discretized using hexahedral quadratic (20-node) elements whose largest linear dimension is 30 times smaller than the half-width of the fault zone. Two sets of simulations are performed for each profile across the target fault zones: one in which the depth of the low-rigidity layer is assumed to be equal to the width of the layer, and another in which the depth of the low-rigidity layer is much greater than the width of the layer. The horizontal and vertical surface displacements due to the compliant fault zone are projected onto the satellite line of sight using local radar incidence angles and satellite heading.

As one can see from Figure 13, the anomalous LOS displacements around the Pinto Mountain fault are well explained by the compliant fault zone model that fits the co-seismic deformation due to the Hector Mine earthquake. Because the sign of the co-seismic stress perturbations due to the Landers earthquake is different from that due to the Hector Mine earthquake, a good agreement between the data and the model predictions suggests that the fault zone deformation is (1) directly proportional to the perturbing stress, and (2) reversible. Therefore the bulk mechanical properties of rocks composing the fault zone appear to be consistent with linear elasticity. Note that the hypothesized com-

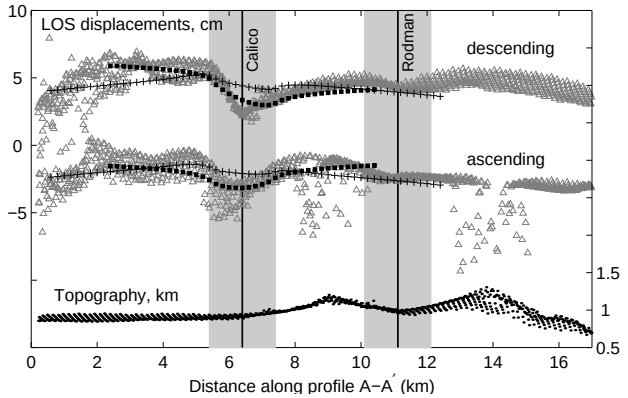

Figure 14. Observed and modeled LOS displacements (left axis) and topography (right axis) along the profile AA′. Notation is the same as in Figure 13. The fault-normal stress change is -1 MPa, and shear stress change is -1.5 MPa (Figure 12).

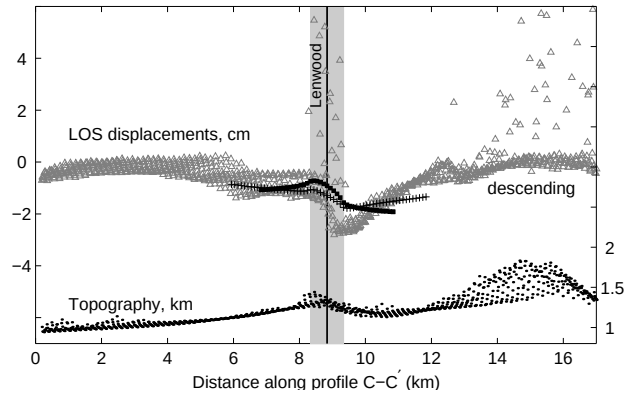

Figure 15. Observed and modeled LOS displacements (descending orbit, left axis) and topography (right axis) along the profile CC′. Notation is the same as in Figure 13. The fault-normal stress change is 0.7 MPa, and shear stress change is -0.6 MPa (Figure 12).

pliant zone is not centered on the geologically deduced trace of the Pinto Mountain fault (Figure 13). This might represent the asymmetric distribution of damaged rocks with respect to the primary rupture surface of the Pinto Mountain fault, or be an artifact of an uncertain fault location around the profile BB′ (Figure 11b).

The compliant fault zone model also reasonably well explains the deformation caused by the Landers earthquake on the Calico and Rodman faults (Figure 11). The model predicts that the amplitude of the fault zone deformation decreases on faults that are further away from the seismic rupture due to the decaying static stress change (Figure 12). Figure 14 shows the observed and modeled LOS displacements along a swath centered on the profile AA′ that crosses the Calico and Rodman faults (Figure 11). As one can see from Figure 14, the anomalous LOS displacements across the Calico fault are greater than the displacements across the Rodman fault, contrary to the deformation pattern induced by the Hector Mine earthquake [*Fialko et al.*, 2002], and in qualitative agreement with the compliant fault zone model. The theoretical LOS displacements are computed using the approach described above. The co-seismic loading of the Calico and Rodman faults by the Landers earthquake is rather complicated due to their proximity to the main rupture, and the conjugate left-lateral faults north and south of Iron Ridge that extend toward the presumed compliant fault zones (Figures 4 and 5). To avoid areas with high stress gradients (e.g., near the eastern edges of the North and South Iron Ridge faults, see Figure 12) the profile AA′ is shifted a few kilometers to the south from the location used in the Hector Mine study [*Fialko et al.*, 2002]. The finite element simulations of deformation due to a 2-km wide compliant zone centered on the Calico fault are in general agreement with the observed LOS displacements from the ascending and descending orbits (Figure 14). For both the Calico and the Pinto Mountain faults, the modeling results suggest that the compliant fault zones are likely to have a depth extent in excess of a few kilometers (cf. squares and pluses in Figures 13 and 14).

The same mechanism may be also responsible for the observed strain localization on other faults of the Eastern California Shear Zone. For example, previous InSAR studies [e.g., *Zebker et al.*, 1994; *Price and Sandwell*, 1998] have documented small-scale displacements on the Lenwood fault (west of the Camp Rock fault, see Figure 11). These displacements have been interpreted as indicating shallow left-lateral slip on the right-lateral Lenwood fault. Figure 15 shows the observed variations in the LOS displacements from a profile CC′ spanning the Lenwood fault (Figure 11). The wavelength of the displacement anomaly across the Lenwood fault is reduced compared to those associated with the Calico and Pinto Mountain faults, ostensibly indicating a narrower fault zone. Color symbols in Figure 15 denote the results of ad-hoc finite element simulations assuming a fault zone width of 1 km. As one can see from Figure 15, the theoretical LOS displacements

are in qualitative agreement with the observed ones, implying that the compliant fault zone hypothesis is consistent with the data. The data from the ascending orbit are not shown in Figure 15 because they are noisy, but the overall sense of the LOS displacements in the ascending interferogram (Figure 11b) is consistent with the proposed model. The fact that the model somewhat underestimates the amplitude of the observed LOS displacements (Figure 15) suggests that the rigidity contrast between the fault zone rocks and the crust around the Lenwood fault is likely greater than a factor of two. Taken together, results shown in Figures 11-15 indicate that the fault zone properties (i.e., the effective width of the compliant layer, and elastic moduli) may vary significantly.

5. Discussion

The 1992 Landers and the 1999 Hector Mine earthquakes are so far the only events for which the space geodetic data are sufficient to provide a well-resolved 3-D description of the large-scale surface deformation (Figure 2, [*Fialko et al.*, 2001b]). The detailed measurements of the co-seismic displacements due to these events therefore provide a unique insight into the bulk constitutive properties of the upper crust. The most prominent zeroth-order feature of the surface deformation field is a "butterfly" pattern of the horizontal displacements (Figure 2f). This pattern is a consequence of, and a direct observational evidence for the double-couple (i.e., zero net torque) nature of the seismic source [*Burridge and Knopoff*, 1964; *Aki and Richards*, 1980]. The co-seismic displacements decay away from the Landers rupture approximately according to a power law, consistent with the overall elastic response of the upper crustal rocks off the fault plane. A more subtle question, however, is whether the elastic deformation is linear. Experimental data and some theoretical arguments suggest that the effective elastic moduli of rocks may depend on the local stress [e.g., *Jaeger and Cook*, 1979; *Chen and Stimpson*, 1993]. Because the crustal rocks contain cracks and other defects on a variety of scales ranging from millimeters to many kilometers, the extensional stresses might result in a partial crack opening, thereby lowering the effective bulk modulus, and resulting in greater displacements compared to those due to the compressive stress changes of the same magnitude. The high resolution space geodetic data may be used to establish whether the effect of the stress-dependent elastic moduli causes appreciable deviations from linear elasticity on a crustal scale. *Peltzer et al.* [1998a] analyzed the co-seismic displacement field due to the 1997 M_w7.6 Manyi earthquake (Tibet, China) using ERS SAR data from one look direction, and inferred a significant asymmetry in the distribution of the fault offsets with respect to the rupture trace. They argued that this asymmetry results from the non-linear response of crustal rocks to the co-seismic stress perturbations through a stress dependence of the effective elastic moduli. The same mechanism has been also invoked to explained deformation due to volcanic sources. For example, *Rubin* [1992] pointed out that models of dike intrusions in Iceland that fit the vertical displacement data tend to underestimate the horizontal deformation. Because dike intrusions clearly occur in an extensional environment, the larger-than-predicted horizontal displacements might be evidence of stress-dependent elastic moduli of upper crustal rocks, although other interpretations are possible [*Rubin*, 1992; *Fialko et al.*, 2001a]. It is important to establish how strongly crustal deformation may deviate from linear elasticity, as the latter is assumed in most of the seismic and geodetic models of the earthquake and volcanic sources.

The previous 3-D observations of the co-seismic deformation due to a large strike-slip earthquake [*Fialko et al.*, 2001b] suggest that the linear elastic approximation may be adequate. In particular, the horizontal co-seismic displacements due to the Hector Mine earthquake are predominantly anti-symmetric with respect to the surface rupture, and do not exhibit asymmetric increases in the extensional quadrants that would be predicted if elastic models were stress-dependent. In fact, some asymmetric increases in the horizontal displacements are apparent in the compressional south-east quadrant of the Hector Mine earthquake, and have been attributed to the along-strike variations in the fault dip angle [*Fialko et al.*, 2001b]. The data from the Landers earthquake (Figure 2) are consistent with these observations. Although the data coverage for the Landers earthquake is not as complete as in the case of the Hector Mine earthquake, it can be seen in Figure 2f that the displacements in the extensional north-east quadrant do not exceed (and if anything are smaller than) those in the compressional north-west quadrant. Greater horizontal displacements in the north-west quadrant of the Landers earthquake may be due to either an arcuate fault geometry, or a small westward dip of the northern part of the Landers rupture (or both). Figure 16 illustrates the asymmetry in the surface displacement field that arises from deviations of the strike-slip fault geometry from (a) planarity and (b) vertical orientation. Because the northern section of the Landers rupture is at a high angle to the re-

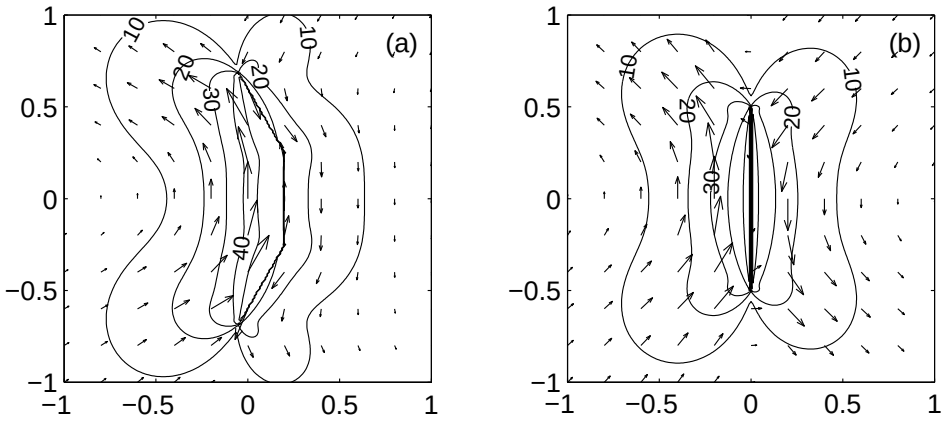

Figure 16. Horizontal displacement field on the surface of a homogeneous elastic half-space due to (a) three vertical strike-slip dislocations approximating a curved fault, and (b) a steeply dipping strike-slip dislocation (dip angle of 80°W). Contours denote the amplitude (in percent of the total slip), and arrows show the displacement direction. The down-dip dimension of the dislocations is 0.5 units of length.

gional compression axis [*Sauber et al.*, 1986; *Lisowski et al.*, 1991; *Unruh et al.*, 1996], the latter interpretation implies that the rupture might acquire a small thrust component as it was propagating to the north, and progressively rotating counter-clock wise to the west. The vertical displacement data indicate an uplift of the west side of the Camp Rock fault (Figure 2e), consistent with thrusting on a westward-dipping fault. However, the assumption of a non-vertical fault is not supported by the aftershock data (Figure 4). It is also not warranted by the inversions of the geodetic data (Appendix A, Table 1). The slip inversions indicate that the asymmetry in the horizontal displacements can be well explained by the fault curvature. Therefore, I conclude that the large-scale co-seismic deformation due to the Landers earthquake is consistent with a model of a vertical strike-slip fault in a linearly elastic half-space. A comparison between the co-seismic strain induced by the Landers and Hector Mine earthquakes on neighboring faults suggests that linear elasticity may also provide an adequate description of the small-scale deformation within the compliant fault zones (Figures 11-15). In particular, the co-seismic deformation on the Calico and Pinto Mountain faults appears to be reversible, with the deformation amplitude dependent on the magnitude, but independent of the sign of the causal stress change. *Rice* [1992] has suggested that mature faults such as the San Andreas fault in California have a perfectly plastic fault zone with a nearly hydrostatic stress, allowing the fault to develop and maintain high pore fluid pressures. Results presented in the previous section do not lend support for the plastic zone model for faults in the Eastern California Shear Zone. In particular, this is because plastic deformation depends on the absolute stress, and is not invariant with respect to the sign of the stress change.

The inferred direct proportionality between stress and strain on both the crustal scale (Figure 2f), and within the compliant fault zones (Figures 11-15) may be reconciled with laboratory inferences of the stress-dependent elastic moduli [*Jaeger and Cook*, 1979; *Brown et al.*, 1989; *Chen and Stimpson*, 1993] by noting that the reduction in the effective bulk modulus via opening of microcracks requires an absolute tension. The latter may be achieved in situ only when the co-seismic stress perturbation completely relieves the least compressive stress. For the typical seismic stress drops of 0.1-10 MPa [e.g., *Kanamori and Anderson*, 1975; *Abercrombie*, 1995], the maximum depth at which the non-linear effects of stress-dependent elastic moduli might be appreciable is of the order of meters to hundreds of meters. Variations in the constitutive properties within a thin (< 1 km) shallow layer are unlikely to affect the overall co-seismic displacement field at the Earth's surface.

Although the observed response of the fault zone rocks to the co-seismic loading may be satisfactorily explained with the elastic model, the inferred reductions in the effective elastic modulus within the fault zones are presumably a result of prior inelastic deformation. It is reasonable to assume that the deduced decreases in the effective shear modulus are caused by the extensive cracking and damage of rocks adjacent to the primary

slip surface, as observed in the field and theoretically predicted [e.g., *Chester and Chester*, 1998; *Vermilye and Scholz*, 1998; *Lyakhovsky et al.*, 2001; *Sibson*, 2003]. This damage may be caused, for example, by large stress perturbations associated with the passing rupture fronts [e.g., *Rice*, 1980], or aftershocks occurring within a finite volume around the co-seismic slip surface [*Liu et al.*, 2003], and accumulate over many earthquake cycles. The space geodetic observations provide robust constraints on the spatial extent and amount of the earthquake-induced damage within the fault zones. The InSAR data presented in this and previous studies [*Fialko et al.*, 2002] suggest that the width of the damage zones may vary from several hundred meters (e.g., in case of the Lenwood and Emerson faults) up to a few kilometers (in case of the Calico, Rodman, and Pinto Mountain faults). The InSAR observations of the post-seismic collapse along the rupture trace of the Hector Mine earthquake [*Jacobs et al.*, 2002] are also indicative of a kilometer-wide fault zone that is mechanically distinct from the ambient crust. The depth extent of the compliant zones is less certain due to the intrinsic loss of resolution of the geodetic observations with depth, but the data seem to require the compliant zones to be deeper than at least a few kilometers (e.g., Figures 11-15). The reduction in the effective elastic moduli within the fault zones varies from less than a factor of 1.7 [e.g., the Rodman fault, *Fialko et al.*, 2002] to more than a factor of 2 (e.g., the Lenwood fault, Figure 15) of the ambient crust values. These variations in the elastic properties may be interpreted in terms of changes in the micro-crack density or the effective damage parameter [e.g., *O'Connell and Budiansky*, 1974; *Kemeny and Cook*, 1986; *Lyakhovsky et al.*, 2001]. Unfortunately, the effect of the inferred decreases in the fault zone rigidity on the fault strength is not well understood. If the fault strength is proportional to the effective shear modulus of rocks within the fault zone, as suggested by some theoretical arguments [*Jaeger and Cook*, 1979; *Lyakhovsky et al.*, 2001], observations of the compliant fault zones may be direct evidence for a relative weakness [as defined by *Rice*, 1992] of large seismogenic faults.

The presence of massive compliant zones around the relatively young and infrequently slipping faults of the Eastern California Shear Zone is perhaps surprising, given that such zones are not always observed around mature faults such as the San Andreas fault. In particular, the limited seismic [e.g., *Feng and McEvilly*, 1983; *Li et al.*, 1997; *Thurber et al.*, 2003] and geodetic [e.g., *Thatcher and Lisowski*, 1987; *Chen and Freymueller*, 2002] studies of the San Andreas fault indicate that the large compliant zones may be present in some but not all locations along the fault. The observed spatial variability in the fault zone properties may be a result of many factors, including the along-fault variations in petrology and host rock composition, geometric complexities in the fault structure [*Wesnousky*, 1988; *Stirling et al.*, 1996], cumulative damage from past earthquakes, and time-dependent healing in the inter-seismic period [*Li et al.*, 1998, 2003]. The fault zone healing (i.e., a gradual recovery of the effective elastic moduli toward the pre-seismic state) prompts a possibility that the anomalous fault compliance might be a transient feature, essentially characterizing a time since the last earthquake. Preliminary field studies of paleoseismicity on the Calico fault may lend support to this hypothesis. In particular, the available paleoseismic data show that the segment of the Calico fault associated with a large compliant zone (Figure 11) might have been ruptured by a moderate-to-large earthquake as recently as several hundred years ago (Tom Fumal, personal communication, 2003). The observed rates of the post-seismic fault healing [*Li et al.*, 1998, 2003] appear to be too low to allow for a complete recovery of the fault zone rigidity on a time scale of the order of the average earthquake recurrence interval in ECSZ. If so, the compliant zones might be a quasi-permanent feature of young active seismogenic fault zones. Recent observations of "softening" of the Landers fault zone caused by the Hector Mine earthquake [*Vidale and Li*, 2003] demonstrate that the fault zone properties (the effective shear modulus, and perhaps the strength) can be also perturbed by changes in the ambient stress field. This implies that the seismogenic fault zones may experience complex interactions between the tectonic loading, stressing by nearby earthquakes, and time-dependent evolution of the fault zone properties. The resulting spatio-temporal variations in both the crustal stress and strength might exert important controls on the occurrence of earthquakes. In particular, such variations undermine the assumptions behind the simple earthquake recurrence models postulating the time- or size-predictability [e.g., *Shimazaki and Nakata*, 1980; *Scholz*, 1990, p. 243]. Further studies are needed to document the spatial extent and ubiquity of compliant zones around major crustal faults, and understand the possible relationships between the observed reductions in the effective elastic moduli of the fault zone rocks, and the fault strength.

6. Conclusions

The 3-D deformation of the Earth surface caused by the 1992 M_w7.3 Landers earthquake, Southern Cali-

fornia, is analyzed using space geodetic measurements (SAR and GPS). I derive continuous maps of horizontal and vertical displacements due to the earthquake. The far-field co-seismic displacements are a classic representation of a double-couple source in an elastic half-space. The near-field displacements are essentially antisymmetric with respect to the rupture surface, indicative of the linearly elastic deformation. These features of the large-scale co-seismic deformation justify the use of seismic and geodetic models based on the approximation of linear elasticity. The space geodetic data are inverted for the fault geometry and slip distribution using homogeneous and layered elastic half-space models. The preferred slip model for the Landers earthquake that fits the SAR (LOS and AZO) data from the ascending and descending satellite orbits satisfactorily predicts independent observations (e.g., point GPS measurements, and surface slip distribution), and favorably compares to the previous inversions of the seismic and geodetic data. The joint inversions of the seismic and geodetic data may not be an optimal strategy for deriving the slip models of large shallow earthquakes because of the intrinsic trade-offs between the timing and location of slip. Provided that the spatially continuous 3-D geodetic data are available, a more robust approach might be to (1) invert for a static slip model using the geodetic data alone, and (2) use the static slip model as a constraint for the time-dependent inversions of seismic data for the rupture history, and perhaps some details of the static slip at depth.

The InSAR data reveal anomalous strain induced by the Landers earthquake on several neighboring faults; some of the faults (e.g., Calico and Pinto Mountain) have been also strained by the subsequent Hector Mine earthquake [*Fialko et al.*, 2002]. The analysis of the anomalous LOS displacements across these faults supports the hypothesis that the fault motion is due to the presence of macroscopic compliant fault zones having widths up to 2 km, and reductions in the effective shear modulus up to a factor of two or greater. The observed deformation of the compliant fault zones is most likely caused by static stress changes due to the nearby earthquakes, and the reversal of motions on some faults between the earthquakes indicates the linear elasticity of the fault zone material. The fault compliance may result from inelastic deformation (cracking, dilatancy, etc.) generated by previous earthquakes, and might manifest a relative fault weakness with respect to the ambient crust. Once the compliant fault zones are established around active faults, they may be further strained and damaged by changes in the in situ stress (e.g., from nearby earthquakes). Understanding of the evolution of the fault zone properties throughout the pre-, post-, and inter-seismic periods warrants detailed seismic and geodetic studies of the major compliant zones.

Acknowledgments.

I thank John Vidale and Elizabeth Cochran for comments and discussions, and the Associate Editor Yehuda Bock, Wayne Thatcher, and Yong-Gang Li for their helpful reviews. Original SAR data are copyrighted by the European Space Agency, distributed by Eurimage, Italy, and acquired via the WInSAR Consortium with funding from NSF, NASA and USGS. Observation and modeling data used in this study are available from the author. This research was supported by the Southern California Earthquake Center. SCEC is funded by NSF Cooperative Agreement EAR-0106924 and USGS Cooperative Agreement 02HQAG0008. The SCEC contribution number for this paper is 758.

Appendix A: Inversion formalism

To ensure a balanced contribution of different datasets (i.e., LOS, AZO, and GPS data) in a joint inversion, each data set is re-normalized such that the sum of weights assigned to individual data points, w_i, equals unity,

$$\sum_{i=1}^{N} w_i = 1, \tag{A1}$$

where N is the number of points in a particular data set. The assigned data weights w_i are taken to be inversely proportional to the measurement errors σ_i when the latter are available (e.g., for the AZO and GPS data),

$$w_i = \frac{1}{\sigma_i \sum_{j=1}^{N} \frac{1}{\sigma_j}}. \tag{A2}$$

In equation (A2), σ_i corresponds to the 95% confidence limits for the components of a displacement vector inferred from the GPS data, and a geometric mean of errors associated with all pixels in an averaging bin i selected by the variable sampling algorithm (Section 3) for the AZO data. For the LOS displacements the measurement errors are not readily available, and the data points are simply weighed proportionally to a number of pixels in the corresponding averaging bins (Figure 5),

$$w_i = \frac{\sqrt{n_i}}{\sum_{j=1}^{N} \sqrt{n_j}}, \tag{A3}$$

where n_i is the number of pixels in the averaging bin i, and N is the total number of points in the interferogram prior to sub-sampling. Equations (A2) and (A3) are the corrected versions of equations 12 and 13 in *Simons et al.* [2002] (in particular, the latter do not satisfy the condition (A1)).

After the re-normalization (A3) and (A2), the data covariance matrixes are generated by scaling the weights of individual data points, $C_i^j = \alpha_j^{-1} w_i$, where index $j = g, s$ denotes the GPS and SAR data sets, respectively. Factors α_j represent the relative weighting of each data set in a joint inversion. Numerical experiments show that the solutions that satisfy the SAR data from more than two look directions are generally able to predict the GPS data. Therefore the latter are downweighted in the final inversions by choosing $\alpha_s = 1$, and $\alpha_g = 10$ (units of displacements); the best fitting solution is essentially unaffected by the GPS data.

For a given fault geometry, the inverse problem represents an overdetermined system of linear equations

$$\begin{aligned} C^s G_s \mathbf{u} &= C^s \mathbf{d_s}, \\ C^g G_g \mathbf{u} &= C^g \mathbf{d_g}, \\ \alpha_s^{-1} \nabla \mathbf{u} &= 0, \end{aligned} \tag{A4}$$

where $\mathbf{d}$ are the data vectors, and $G_{s,g}$ are the respective Green's functions. The SAR data ($\mathbf{d_s}$) are de-trended prior to the inversion using a procedure described in Section 2. The last equation in system (A4) is the smoothing operator that minimizes the slip gradient, α_s^{-1} being the effective damping coefficient. The smoothing is implemented using finite difference quadratures for a first spatial derivative of slip. To further regularize the problem, I require that the strike slip is right-lateral on the Landers rupture (sub-faults 1-6, Figure 4), and left-lateral on the Big Bear and Iron Ridge faults (sub-faults 7-9). No constraints are imposed on the dip slip component. The Green's functions are computed using solutions for a finite rectangular dislocation in an isotropic elastic half-space [e.g., *Okada*, 1985], and point dislocations in a horizontally stratified half-space [*Wang et al.*, 2003]. All geometric parameters of the model sub-faults except the dip angle are assumed to be constant. The initial model assumes vertically dipping sub-faults. The inversion performs a forward grid search for the best-fitting fault dip angles. At each step I recalculate the appropriate Green's functions G_j, invert the system (A4), and evaluate the least squares residual between the model and the data. I accept changes in the fault geometry if they produce more than one percent reduction in the root mean square (rms) misfit between the model and the data. The final model geometry (see Table 1) does not significantly differ from the initial one, indicating that the non-vertical dip angles are not required by the data. There is a slight indication that the rupture plane of the Big Bear earthquake may be dipping to the South, and the northern section of the Landers rupture (on the Camp Rock fault) may be dipping to the West.

Appendix B: Model resolution tests

A number of numerical experiments are performed to estimate the resolving power of the available geodetic data and the inversion scheme. After the initial fault geometry is specified using the surface rupture, aftershock, and SAR data (Figure 4), I generate the synthetic SAR and GPS data due to a unit slip on each patch of the discretized fault model (e.g., Figure 8), while the rest of the fault is assumed to have no slip. These synthetic "Green function" data are then inverted for the slip distribution on the entire fault. The fraction of slip recovered on the corresponding non-zero slip patch is a good measure of how well the patch is resolved with the given data. For the equi-dimensional fault discretization, the model resolution significantly decreases with the increasing depth. To compensate for this decay, I adjust the geometric factor that governs the increase in the patch size with depth such that the patch resolution is not smaller than 0.4. After a suitable discretization scheme is chosen, I perform a "checker-board" test in which I simulate the SAR and GPS data using a model with an extremely heterogeneous slip. Figure B1 shows the input model used to calculate the synthetic data. A pure strike slip of 7 meters is applied to simulate several "asperities" on the Landers fault, with no offsets in the intervening areas. The synthetic data due to the model shown in Figure B1 are calculated at the locations of the data pixels in the LOS and AZO maps from the ascending and descending orbits (Figure 2), and at the GPS sites (Figure 10a). A random noise of 2% of the local signal amplitude is added to the synthetic data. The synthetic SAR data are sub-sampled in the same fashion as the observed data, and inverted using the same parameters as used for deriving the solutions shown in Figures 8 and 9. The results of the synthetic inversion are shown in Figure B2. As one can see from a comparison of Figures B1 and B2, even with the limited coverage of SAR data (Figure 2) one is able to reasonably well resolve the regions of high and low slip on the Landers fault model. The slip amplitude is somewhat reduced in the inversion due to smearing. Note that the trade-off between the strike-slip and dip-slip components of displacements in the inverse model is quite small. Best constrained is the shallow fault structure, as one might expect.

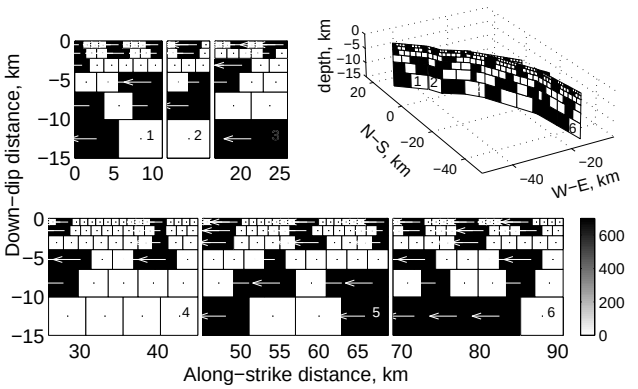

Figure B1. Synthetic slip model used in the resolution test.

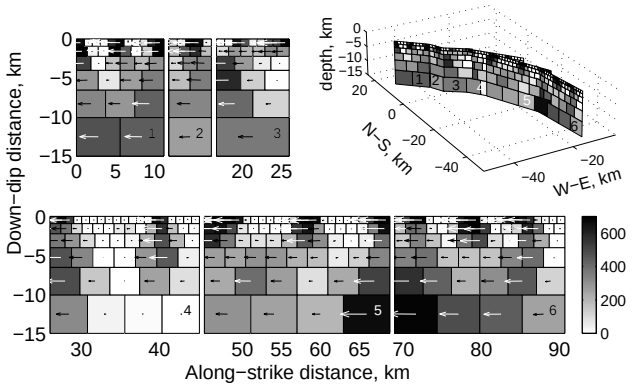

Figure B2. Slip distribution obtained from the inversion of synthetic data generated using a test model shown in Figure B1.

References

Abercrombie, R., Earthquake source scaling relationships from -1 to 5 M_L using seismograms recorded at 2.5-km depth, *J. Geophys. Res.*, *100*, 24,015–24,036, 1995.

Aki, K., and P. G. Richards, *Quantitative Seismology: Theory and Methods, I and II*, 577 pp., W. H. Freeman, San Francisco, Calif., 1980.

Bock, Y., et al., Detection of crustal deformation from the Landers earthquake sequence using continuous geodetic measurements, *Nature*, *361*, 337–340, 1993.

Bodin, P., R. Bilham, J. Behr, J. Gomberg, and K. Hudnut, Slip triggered on southern california faults by the 1992 joshua-tree, landers, and big-bear earthquakes, *Bull. Seism. Soc. Am.*, *84*, 806–816, 1994.

Brown, E., J. Bray, and F. Santarelli, Influence of stress-dependent elastic-moduli on stresses and strains around axisymmetric boreholes, *Rock Mech. Rock Eng.*, *22*, 189–203, 1989.

Burgmann, R., P. Rosen, and E. Fielding, Synthetic aperture radar interferometry to measure Earth's surface topography and its deformation, *Annu. Rev. Earth Planet. Sci.*, *28*, 169–209, 2000.

Burridge, R., and L. Knopoff, Body force equivalents for seismic dislocations, *Bull. Seism. Soc. Am.*, *54*, 1875–1888, 1964.

Chen, Q., and J. Freymueller, Geodetic evidence for a near-fault compliant zone along the San Andreas fault in the San Francisco Bay area, *Bull. Seismol. Soc. Am.*, *92*, 656–671, 2002.

Chen, R., and B. Stimpson, Interpretation of indirect tensile-strength tests when moduli of deformation in compression and in tension are different, *Rock Mech. Rock Eng.*, *26*, 183–189, 1993.

Chester, F. M., and J. S. Chester, Ultracataclasite structure and friction processes of the Punchbowl fault, San Andreas system, California, *Tectonophysics*, *295*, 199–221, 1998.

Dahlen, F. A., and J. Tromp, *Theoretical Global Seismology*, 944 pp., Princeton University Press, Princeton, New Jersey, 1998.

Farr, T., and M. Kobrick, Shuttle Radar Topography Mission produces a wealth of data, *AGU Eos*, *81*, 583–585, 2000.

Feng, R., and T. McEvilly, Interpretation of seismic-reflection profiling data for the structure of the San-Andreas fault zone, *Bull. Seism. Soc. Am.*, *73*, 1701–1720, 1983.

Fialko, Y., Evidence of fluid-filled upper crust from observations of post-seismic deformation due to the 1992 M_w7.3 Landers earthquake, *J. Geophys. Res.*, submitted, 2004.

Fialko, Y., and M. Simons, Deformation and seismicity in the Coso geothermal area, Inyo County, California: Observations and modeling using satellite radar interferometry, *J. Geophys. Res.*, *105*, 21,781–21,793, 2000.

Fialko, Y., Y. Khazan, and M. Simons, Deformation due to a pressurized horizontal circular crack in an elastic half-space, with applications to volcano geodesy, *Geophys. J. Int.*, *146*, 181–190, 2001a.

Fialko, Y., M. Simons, and D. Agnew, The complete (3-D) surface displacement field in the epicentral area of the 1999 M_w7.1 Hector Mine earthquake, southern California, from space geodetic observations, *Geophys. Res. Lett.*, *28*, 3063–3066, 2001b.

Fialko, Y., D. Sandwell, D. Agnew, M. Simons, P. Shearer, and B. Minster, Deformation on nearby faults induced by the 1999 Hector Mine earthquake, *Science*, *297*, 1858–1862, 2002.

Freymueller, J., N. E. King, and P. Segall, The co-seismic slip distribution of the Landers earthquake, *Bull. Seismol. Soc. Am.*, *84*, 646–659, 1994.

Gabriel, A. K., R. M. Goldstein, and H. A. Zebker, Mapping small elevation changes over large areas: Differential radar interferometry, *J. Geophys. Res.*, *94*, 9183–9191, 1989.

Goldstein, R. M., H. Engelhardt, B. Kamb, and R. Frolich, Satellite radar interferometry for monitoring ice sheet motion: Application to an Antarctic ice stream, *Science*, *262*, 1525–1530, 1993.

Hauksson, E., et al., The 1992 Landers earthquake sequence: Seismological observations, *J. Geophys. Res.*, *98*, 19,835–19,858, 1993.

Hernandez, B., F. Cotton, and M. Campillo, Contribution of radar interferometry to a two-step inversion of the kinematic process of the 1992 Landers earthquake, *J. Geophys. Res.*, *104*, 13,083–13,099, 1999.

Hudnut, K. W., et al., Co-seismic displacements in the Landers sequence, *Bull. Seismol. Soc. Am.*, *84*, 625–645, 1994.

Jacobs, A., D. Sandwell, Y. Fialko, and L. Sichoix, The 1999 (M_w7.1) Hector Mine, California, earthquake: Near-field postseismic deformation from ERS interferometry, *Bull. Seism. Soc. Am.*, *92*, 1433–1442, 2002.

Jaeger, J., and N. Cook, *Fundamentals of Rock Mechanics*, 2 ed., 585pp., Chapman & Hall, London, 1979.

Jones, L., and D. Helmberger, Earthquake source parameters and fault kinematics in the eastern California shear zone, *Bull. Seism. Soc. Am.*, *88*, 1337–1352, 1998.

Jonsson, S., H. Zebker, P. Segall, and F. Amelung, Fault slip distribution of the 1999 M_w 7.1 Hector Mine, California, earthquake, estimated from satellite radar and GPS measurements, *Bull. Seism. Soc. Am.*, *92*, 1377–1389, 2002.

Kanamori, H., and D. L. Anderson, Theoretical basis of some empirical relations in seismology, *Bull. Seis. Soc. Amer.*, *65*, 1073–1095, 1975.

Kanamori, H., H. K. Thio, D. Dreger, E. Hauksson, and T. Heaton, Initial investigation of the Landers, California, earthquake of 28 June 1992 using TERRAscope, *Geophys. Res. Lett.*, *19*, 2267–2270, 1992.

Kemeny, J., and N. Cook, Effective moduli, nonlinear deformation and strength of a cracked elastic solid, *Int. J. Rock Mech. Min. Sci.*, *23*, 107–118, 1986.

Kostrov, B. V., and S. Das, *Principles of earthquake source dynamics*, 286 pp., Cambridge University Press, Cambridge, UK, 1988.

Li, Y., W. Ellsworth, C. Thurber, P. Malin, and K. Aki, Fault-zone guided waves from explosions in the San Andreas fault at Parkfield and Cienega Valley, California, *Bull. Seism. Soc. Am.*, *87*, 210–221, 1997.

Li, Y., J. Vidale, K. Aki, F. Xu, and T. Burdette, Evidence of shallow fault zone strengthening after the 1992 M7.5 Landers, California, earthquake, *Science*, *279*, 217–219, 1998.

Li, Y., J. Vidale, S. Day, D. Oglesby, and E. Cochran, Postseismic fault healing on the rupture zone of the 1999 M 7.1 Hector Mine, California, earthquake, *Bull. Seism. Soc. Am.*, *93*, 854–869, 2003.

Lisowski, M., J. Savage, and W. H. Prescott, The velocity field along the San Andreas fault in central and southern California, *J. Geophys. Res.*, *96*, 8369–8389, 1991.

Liu, J., K. Sieh, and E. Hauksson, A structural interpretation of the aftershock "Cloud" of the 1992 M_w 7.3 Landers earthquake, *Bull. Seism. Soc. Am.*, *93*, 1333–1344, 2003.

Lyakhovsky, V., Y. Ben-Zion, and A. Agnon, Earthquake cycle, fault zones, and seismicity patterns in a rheologically layered lithosphere, *J. Geophys. Res.*, *106*, 4103–4120, 2001.

Massonnet, D., and K. Feigl, Radar interferometry and its application to changes in the Earth's surface, *Rev. Geophys.*, *36*, 441–500, 1998.

Massonnet, D., M. Rossi, C. Carmona, F. Adragna, G. Peltzer, K. Feigl, and T. Rabaute, The displacement field of the Landers earthquake mapped by radar interferometry, *Nature*, *364*, 138–142, 1993.

O'Connell, R. J., and B. Budiansky, Seismic velocities in dry and saturated cracked solids, *J. Geophys. Res.*, *79*, 5412–5426, 1974.

Okada, Y., Surface deformation due to shear and tensile faults in a half-space, *Bull. Seismol. Soc. Am.*, *75*, 1135–1154, 1985.

Peltzer, G., F. Crampe, and G. King, Evidence of nonlinear elasticity of the crust from the m_w7.6 manyi (tibet) earthquake, *Science*, *286*, 272–276, 1998a.

Peltzer, G., P. Rosen, F. Rogez, and K. Hudnut, Poroelastic rebound along the Landers 1992 earthquake surface rupture, *J. Geophys. Res.*, *103*, 30,131–30,145, 1998b.

Peyrat, S., K. Olsen, and R. Madariaga, Dynamic modeling of the 1992 Landers earthquake, *J. Geophys. Res.*, *106*, 26,467–26,482, 2001.

Price, E., and D. T. Sandwell, Small-scale deformations associated with the 1992 Landers, California, earthquake mapped by synthetic aperture radar interferometry phase gradients, *J. Geophys. Res.*, *103*, 27,001–27,016, 1998.

Reid, H., The mechanism of the earthquake, in *The California Earthquake of April 19, 1906*, vol. 2, edited by R. S. I. Comm., Carnegie Institution, Washington, D.C., 1910.

Rice, J. R., The mechanics of earthquake rupture, in *Physics of the Earth's Interior*, edited by A. M. Dziewonski and E. Boschi, pp. 555–649, North-Holland, Amsterdam, 1980.

Rice, J. R., Fault stress states, pore pressure distribution, and the weakness of the San Andreas Fault, in *Fault mechanics and transport properties of rocks*, edited by B. Evans and T. Wong, pp. 475–503, Academic, San Diego, CA, USA, 1992.

Rosen, P., S. Hensley, I. Joughin, F. Li, S. Madsen, E. Rodriguez, and R. Goldstein, Synthetic aperture radar interferometry, *Proc. of the IEEE*, *88*, 333–382, 2000.

Rubin, A. M., Dike-induced faulting and graben subsidence in volcanic rift zones, *J. Geophys. Res.*, *97*, 1839–1858, 1992.

Rymer, M., Triggered surface slips in the Coachella Valley area associated with the 1992 Joshua Tree and Landers, California, earthquakes, *Bull. Seism. Soc. Am.*, *90*, 832–848, 2000.

Sandwell, D., L. Sichoix, D. Agnew, Y. Bock, and J.-B. Minster, Near real-time radar interferometry of the M_w 7.1 Hector Mine Earthquake, *Geophys. Res. Lett.*, *27*, 3101–3104, 2000.

Sauber, J., W. Thatcher, and S. Solomon, Geodetic measurement of deformation in the central Mojave desert, California, *J. Geophys. Res.*, *91*, 2683–2693, 1986.

Savage, J., Displacement field for an edge dislocation in a layered half-space, *J. Geophys. Res.*, *103*, 2439–2446, 1998.

Savage, J., and J. Svarc, Postseismic deformation associated with the 1992 M_w=7.3 Landers earthquake, southern California, *J. Geophys. Res.*, *102*, 7565–7577, 1997.

Scholz, C. H., *The mechanics of earthquakes and faulting*, 439 pp., Cambidge Univ. Press, New York, NY, 1990.

Shen, Z., D. Jackson, Y. Feng, M. Cline, M. Kim, P. Fang, and Y. Bock, Postseismic deformation following the Landers earthquake, California, 28 June 1992, *Bull. Seism. Soc. Am.*, *84*, 780–791, 1994.

Shimazaki, K., and T. Nakata, Time-predictable recurrence model for large earthquakes, *Geophys. Res. Lett.*, *7*, 279–282, 1980.

Sibson, R. H., Thickness of the seismic slip zone, *Bull. Seism. Soc. Am.*, *93*, 1169–1178, 2003.

Sieh, K., et al., Near-field investigations of the Landers earthquake sequence, *Science*, *260*, 171–176, 1993.

Simons, M., Y. Fialko, and L. Rivera, Coseismic deformation from the 1999 M_w7.1 Hector Mine, California, earthquake, as inferred from InSAR and GPS observations, *Bull. Seism. Soc. Am.*, *92*, 1390–1402, 2002.

Smith, B., and D. Sandwell, Accuracy and resolution of shuttle radar topography mission data, *Geophys. Res. Lett.*, *30*, art. no.–1467, 2003.

Stirling, M. W., S. G. Wesnousky, and K. Shimazaki, Fault trace complexity, cumulative slip, and the shape of the magnitude-frequency distribution for strike-slip faults: a global survey, *Geophys. J. Int.*, *124*, 833–868, 1996.

Thatcher, W., and M. Lisowski, Long-term seismic potential of the San-Andreas fault southeast of San-Francisco, California, *J. Geophys. Res.*, *92*, 4771–4784, 1987.

Thurber, C., S. Roecker, K. Roberts, M. Gold, L. Powell, and K. Rittger, Earthquake locations and three-dimensional fault zone structure along the creeping section of the San Andreas fault near Parkfield, CA: Preparing for SAFOD, *Geophys. Res. Lett.*, *30*, art. no.–1112, 2003.

Unruh, J. R., R. J. Twiss, and E. Hauksson, Seismogenic deformation field in the Mojave block and implications for tectonics of the eastern California shear zone, *J. Geophys. Res.*, *101*, 8335–8361, 1996.

Vermilye, J., and C. Scholz, The process zone: A microstructural view of fault growth, *J. Geophys. Res.*, *103*, 12,223–12,237, 1998.

Vidale, J., and Y. Li, Damage to the shallow Landers fault from the nearby Hector Mine earthquake, *Nature*, *421*, 524–526, 2003.

Vvedenskaya, A., Determination of displacement fields for earthquakes by means of the dislocation theory, *Izv. Akad. Nauk. SSSR. Ser. Geophys.*, *3*, 277–284, (in Russian), 1959.

Wald, D. J., and T. H. Heaton, Spatial and temporal distribution of slip for the 1992 Landers, California, earthquake, *Bull. Seismol. Soc. Am.*, *84*, 668–691, 1994.

Wang, R., F. Martin, and F. Roth, Computation of deformation induced by earthquakes in a multi-layered elastic crust - FORTRAN programs EDGRN/EDCMP, *Comp. Geosci.*, *29*, 195–207, 2003.

Wesnousky, S., Seismological and structural evolution of strike- slip faults, *Nature*, *335*, 340–342, 1988.

Wright, T., E. Fielding, and B. Parsons, Triggered slip: observations of the 17 August 1999 Izmit (Turkey) earthquake using radar interferometry, *Geophys. Res. Lett.*, *28*, 1079–1082, 2001.

Zebker, H. A., P. A. Rosen, R. M. Goldstein, A. Gabriel, and C. L. Werner, On the derivation of coseismic displacement–fields using differential radar interferometry – the Landers earthquake, *J. Geophys. Res.*, *99*, 19,617–19,634, 1994.

Zhu, L., and L. Rivera, A note on the dynamic and static displacements from a point source in multilayered media, *Geophys. J. Int.*, *148*, 619–627, 2002.

Y. Fialko, Institute of Geophysics and Planetary Physics, Scripps Institution of Oceanography, University of California San Diego, La Jolla, CA 92093. (e-mail: fialko@radar.ucsd.edu)

This preprint was prepared with AGU's LaTeX macros v5.01, with the extension package 'AGU^{++}' by P. W. Daly, version 1.6b from 1999/08/19.